




Influence of Braiding Angle on Multiple Impact Damages of 3-D Braided Composite along Longitudinal Direction

Xingzhong Gao¹ · Amna Siddique¹ · Baozhong Sun¹ · Bohong Gu¹ 

Received: 9 April 2019 / Accepted: 5 June 2019 / Published online: 2 July 2019

© Springer Nature B.V. 2019

Abstract

This paper reports deformation and damage evolutions of three-dimensional (3-D) braided composite with different braiding angles under multiple impact compression along longitudinal direction. Braided composites with braiding angle of 15°, 26° and 37° have been prepared for the compression tests. The impact compression test was conducted on a split Hopkinson pressure bar (SHPB) along longitudinal direction. A high-speed camera was used to record damage development. A meso-scale finite element model has been established to simulate damage processes. The results show that the damage of composites occurs mainly in the first three impacts. For the 15° sample, damage of yarns and interface dominates the failure mechanisms at the first impact. For the 26° and 37° samples, the resin fracture and interface de-bonding lead to compressive failure at the first impact. Breakage and dislocation of yarns occurred for 15° sample during the subsequent two impacts, whereas it still keeps good structural integrity for 26° and 37° samples. The angle between adjacent yarns increased for the 26° sample and the yarns just tightened each other for 37° sample. Ductile damage is the primary damage mode for both yarns and resin during the multiple impacts.

Keywords 3-D braided composite · Multiple impact compression · Finite element analysis (FEA) · Split Hopkinson pressure bar (SHPB) · High-speed camera

1 Introduction

Textile preform based composite materials have been widely applied to electromagnetic [1–3], thermoelectric [4] and mechanical [5, 6] areas. As a specific textile composite, three-dimensional (3-D) braided composite has also been widely used for aerospace, automotive and structure engineering due to its high impact resistance, damage tolerance and high strength-weight ratio [7–9]. It is inevitable for composites to undertake high impact compression load in

✉ Bohong Gu
gubh@dhu.edu.cn

¹ College of Textiles, Donghua University, Shanghai 201620, China

service. Dynamic loading response of composite is quite different from static load [10–12]. Dynamic response of braided composite has gained considerable research interest in recent years. Mechanical property in longitudinal and transverse direction weakened with increasing braiding angle [13], but strengthened in the through-thickness direction [14]. Yarns breakage, resin crack, yarns buckling and interface debonding are the main failure modes during impact processes [15–17]. Zhou [18] found the cracks nucleate in the weak areas and propagate along the path of least resistance between yarns for low impact velocity. For high impact velocities, cracks develop along a relatively straight path with fiber breakage under high shear and tensile stress. The similar result was also found by Zhang [19] in 3-D braided composite under transverse impact loading. Li [20] found the most damage occurred at the zone between punch back surface and the middle of the thickness for braided composite under impact shear loading. These researches are focused on only single impact; however, composites always go through multiple-pulse compressions under impact load. The damage evolutions and mechanisms may differ during each impact compression.

There is some literature published to investigate dynamic response of composites under multiple-pulse impact load. Lai [21] studied the properties of functionally graded cement composite targets subjected to three projectile impacts. It proved that the penetration depth, crater diameter and concrete damage increased with the number of impacts. Wu [22] tested the performance of Hard-Soft-Hard (HSH) composite under multiple impacts. The result indicates that the major cracks at the top HSH layer after the first impact was detrimental. The cracks widened, propagated and the sample was finally broken into pieces upon the second impact. Li [23] researched the resistance of hybrid fiber ultrahigh toughness cement composites under multiple impacts. The results showed the specimen with 1.0% steel fiber sustained the largest number of impacts. However, the structure of these composites is different from the braided composite. Damage evolution and mechanisms of braided composite will be completely different from these composites.

Zhou [24] researched the transverse impact behaviors of braided composite tube within four impacts. The result shows the stress of the tube amplified as the number of impact cycles increased. The authors of this paper [25] numerically and experimentally studied the damage development and mechanisms of 3-D braided composite under multiple-pulse impact load along transverse direction. Mechanical behavior of anisotropic composite under longitudinal compressive load is quite different from that under transverse compressive load. The transverse compressive modulus and strength are considerably lower than the longitudinal compressive modulus and strength [26, 27]. The damage mode of fiber reinforcement is the delamination between fabric layers in longitudinal direction, while it is shear failure in the transverse direction [28]. The velocity of stress wave in preform is slower in longitudinal compression than transverse compression. The energy absorbed under transverse impact compression load is much higher than that under longitudinal impact compression load [29]. Thus, dynamic response of 3-D braided composite during each impact compression under multiple impacts along longitudinal direction may be not the same as transverse direction. Further study is needed for revealing the directional differences.

We prepared 3-D braided composite samples with braiding angle of 15°, 26° and 37° to investigate multiple impact deformation and damage along longitudinal direction. Dynamic tests were carried out on split Hopkinson pressure bar (SHPB). A high-speed camera system was used to capture damage evolution information of composite during each impact pulse. We have also developed a finite element model at meso-scale structure level to simulate the damage evolutions. Differences of damage evolution and damage mechanisms among each impact have been revealed. The effect of braiding angle on damage evolution and mechanisms

has also been analyzed. Energy absorption and failure modes during each impact are discussed. We hope this effort could be extended to the optimization of the 3-D braided composite under multiple impact compressions.

2 Experimental

2.1 Materials Preparation

A four-step braiding machine was used to prepare braided preforms with different braiding angles. The braiding angle was changed by controlling the beating force that makes the structure more compact at the end of a braiding cycle. Elastic parameters of carbon fiber tows (supplied by Toray Inc. (Japan)) used in the preparation are listed in Table 1. The resin (a kind of bisphenol A epoxy vinyl) was impregnated into the braided preform with vacuum-assisted resin transfer molding process. The mechanical properties of resin are listed in Table 2. The curing temperature is 90 °C for 2 h, 110 °C for 1 h and 130 °C for 4 h. Based on the ASTM 6856–03 standard, the composites were cut into a cube in 12 mm × 12 mm × 12 mm (Fig. 1) for tests.

2.2 Dynamic Impact Compression Test

Impact tests were conducted with a modified split Hopkinson pressure bar (SHPB). The SHPB test system [30] consists of nitrogen can, striker bar, incident bar, transmission bar, absorption bar and data analysis system. The bars are 30 mm in diameter, 400 mm in length for striker and absorption bar and 20,000 mm in length for incident and transmission bar. The impact velocity is controlled by the magnitude of nitrogen pressure, which is 0.3 MPa used in current research with a corresponding impact velocity magnitude of 11 m/s. The stress-strain as well as strain rate-time curves are finally obtained through data analysis system. An i-speed 716 high speed camera system (IX cameras Ltd., United Kingdom) with shooting frequency of 100,000 frames per second was used to capture the damage evolution. The strain rate for each impact was around 300/s. Each impact test was repeated at least three samples. Multiple impact compressions [31] will occur in the SHPB test system. Damage information of samples during the first three impact pulses was recorded with high-speed camera system.

3 Finite Element Model

3.1 Geometrical Model

Figure 2a shows the geometrical model of preforms and compression direction. Meso-scale geometrical models were established according to the braided architecture proposed by Li [32].

Table 1 Mechanical parameters of carbon fiber

| Fiber | E_{11} (GPa) | E_{22} (GPa) | E_{33} (GPa) | G_{12} (GPa) | G_{13} (GPa) | G_{23} (GPa) | ν_{12} | ν_{13} | ν_{23} | XT (GPa) | $\rho(\text{g}/\text{cm}^3)$ |
|-----------|-------------------|-------------------|-------------------|-------------------|-------------------|-------------------|------------|------------|------------|-------------|------------------------------|
| T700-12 K | 230 | 14 | 14 | 9 | 9 | 5 | 0.25 | 0.3 | 4.9 | 1.8 | |

Table 2 Mechanical parameters of epoxy resin

| Property | Value |
|------------------------------|-------|
| Density (g/cm ³) | 1.13 |
| Elastic modulus (GPa) | 2.4 |
| Shear modulus (GPa) | 0.89 |
| Compressive strength (MPa) | 102 |
| Tensile strength (MPa) | 80 |
| Shear strength (MPa) | 113 |
| Yield strength (MPa) | 69 |
| Poisson's ratio (MPa) | 0.3 |
| Elongation at break (%) | 5.9 |

The cross section of yarns were assumed to be hexagon based on our previous research [33]. The geometrical model of matrix was created by deducting the preform off from a cube. After that the resin is assembled together with the preform. The geometrical model is of the same size as the test sample.

3.2 Materials Model

The resin is regarded as isotropic solid which obeys J2-isotropic hardening plasticity theory [34]. Braided yarns impregnated with the epoxy resin are considered as unidirectional composite, a transversely isotropic material. The local coordinate system was defined for each yarn in finite element analysis (FEA) as shown in Fig. 2b. Direction 1 denotes the primary direction whereas 2 and 3 directions correspond to the transverse directions. Bridge model developed by Huang [35] was used to calculate elastic parameters of yarns. The change of braiding angle may vary the volume fraction of fiber in the yarns, which can finally lead to different elastic parameters of braided yarns. Thus, the volume fraction of fiber in the yarns was measured to ensure the accuracy of yarn's elastic parameters in FEA. Figure 2c shows the scanning electron microscope (SEM) photo of yarn's cross-section before and after processed by Software Image Pro Plus 6. Table 3 is the fiber volume fraction in braided yarn. Five measurements were conducted and the averaged value was obtained. Table 4 shows the elastic parameters of yarns

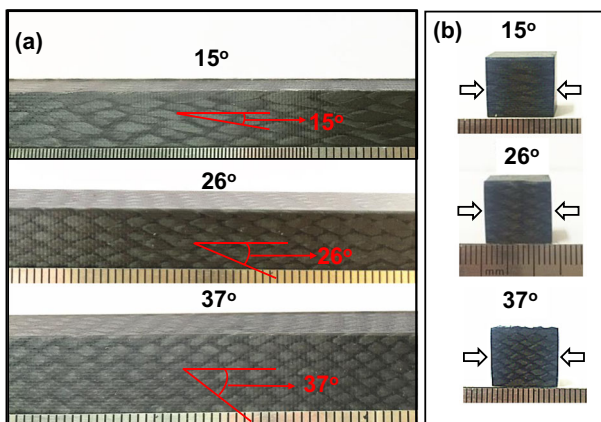


Fig. 1 Three-dimensional braided composite (a) Composites with different braiding angles (b) Sample and compression direction

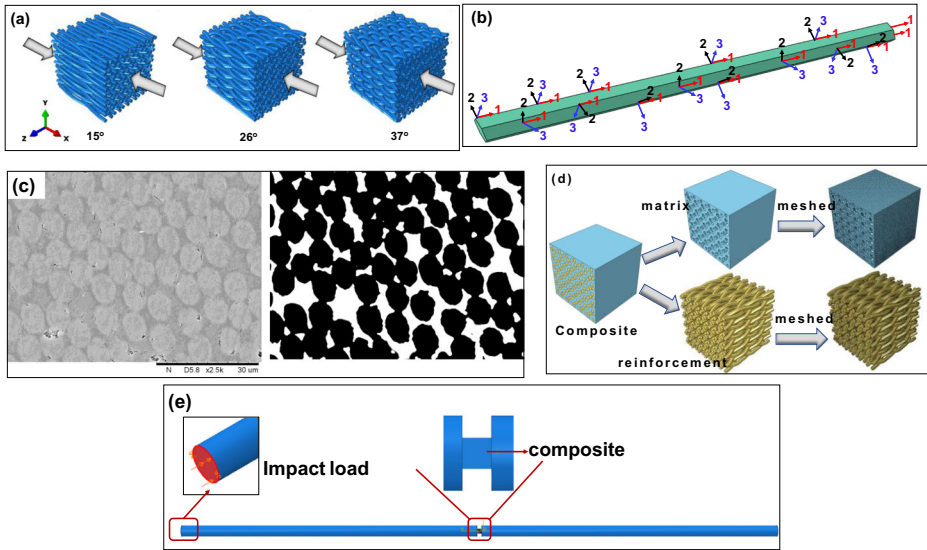


Fig. 2 Finite element model (a) Geometrical model of preforms and compression direction (b) Local system defined in the braided yarn (c) SEM photo of yarn cross-section before and after processed (d) Meshed reinforcement and matrix (e) impact model

based on each volume fraction on Table 3. Hill’s anisotropic plastic model [36] is used to define the yield property of the yarns.

Ductile damage criterion in conjunction with shear damage criterion was used to define the damage initiation. There exists an energy threshold above which ductile and shear damage is likely to occur. Ductile damage initiation is related to pressure stress, while it is shear stress for shear damage initiation. The status of ductile and shear damage in elements can be known by outputting the variable DUCTCRT and SHRCRT in field output of commercial FEA software ABAQUS respectively. The stiffness of elements degrades with a specified law after the damage criterion was met. The elements would be removed from FEA when the stiffness decreases to 1%, which indicates the element completely lost the load-carrying capacity. Surface-based cohesive behavior was used to model the delamination of resin/yarn interface. The damage status of interface was able to be known by outputting the variable CSDMG in field output. More details about damage criterions and cohesive behavior are available to see in reference [31].

3.3 Mesh

Figure 2d, e shows the impact model used in this research. The commercial FEA software ABAQUS was used to develop the 3-D numerical model. The contact between bars and

Table 3 Volume fraction of fiber in the yarns (%)

| Braiding angle (°) | 1# | 2# | 3# | 4# | 5# | Average |
|--------------------|------|------|------|------|------|---------|
| 15 | 68.7 | 71.0 | 69.1 | 70.2 | 75.4 | 70.88 |
| 26 | 73.1 | 73.7 | 71.7 | 73.9 | 71.2 | 72.72 |
| 37 | 75.3 | 73.3 | 71.2 | 80.7 | 79.8 | 76.06 |

Table 4 Elastic parameters of braided yarns

| Braiding angle (°) | E_{11} (GPa) | E_{22} (GPa) | E_{33} (GPa) | G_{12} (GPa) | G_{13} (GPa) | G_{23} (GPa) | ν_{12} | ν_{13} | ν_{23} |
|--------------------|----------------|----------------|----------------|----------------|----------------|----------------|------------|------------|------------|
| 15 | 163.93 | 7.7 | 7.7 | 3.36 | 3.36 | 2.80 | 0.28 | 0.28 | 0.4 |
| 26 | 166.67 | 7.96 | 7.96 | 3.51 | 3.51 | 2.91 | 0.27 | 0.27 | 0.4 |
| 37 | 175.44 | 8.45 | 8.45 | 3.84 | 3.84 | 3.12 | 0.26 | 0.26 | 0.39 |

sample was defined as ‘surface to surface contact’. A cohesive behavior is implemented at resin/yarn interface. The resin was meshed with the element type of ‘C3D4’ while the yarns

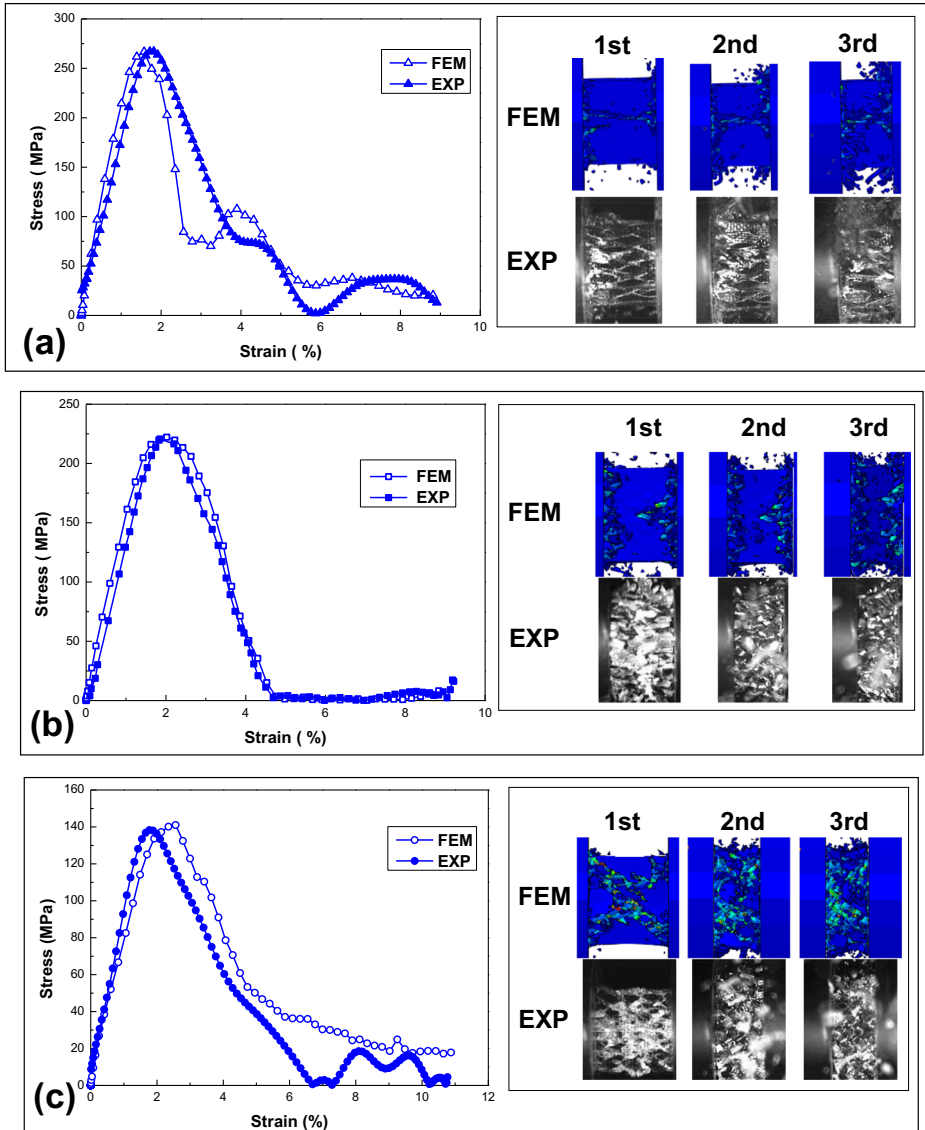


Fig. 3 Comparison of results (stress-strain curve and damage morphology at each impact) obtained from test and simulation (a) 15° sample; (b) 26° sample (c) 37° sample

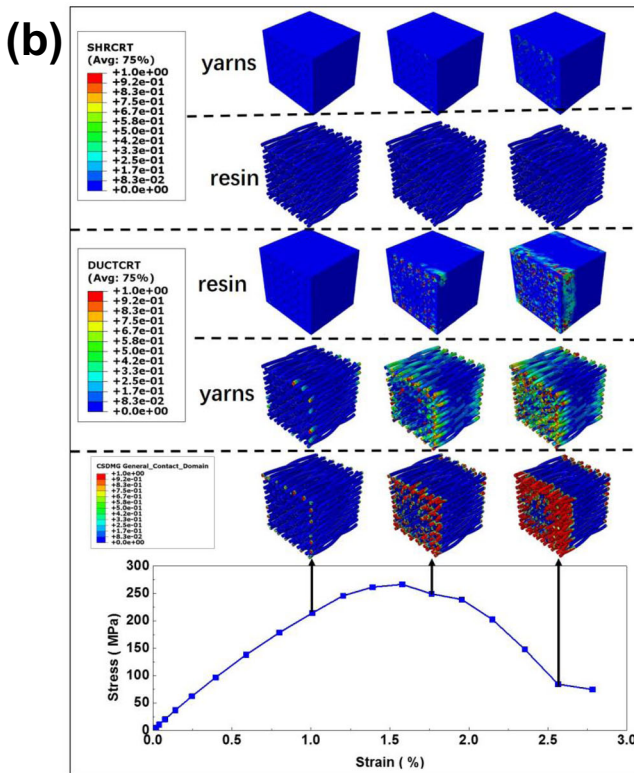
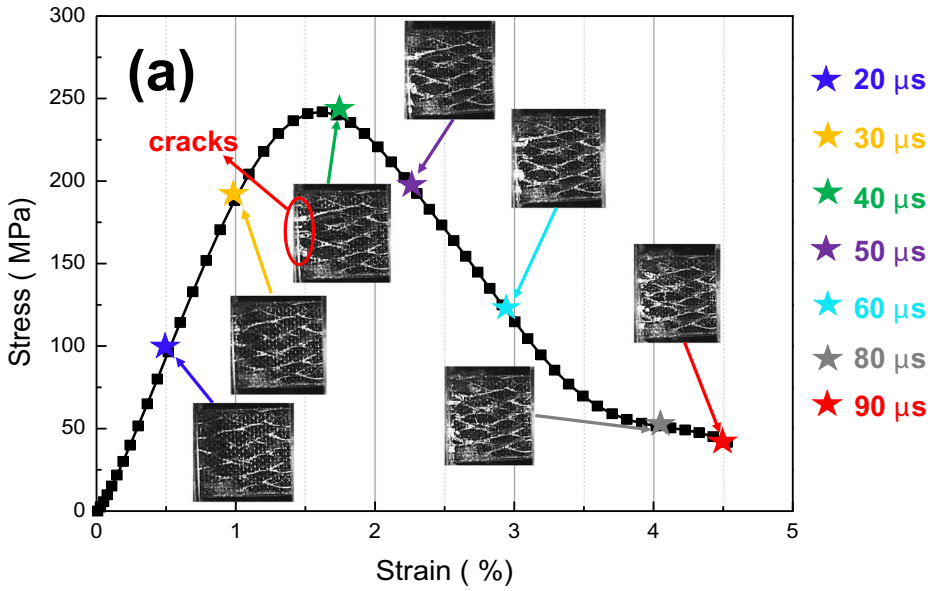


Fig. 4 Failure analysis of 15° sample at the first impact (a) Test results of damage evolution (b) Damage simulation of composite components (yarns, resin and interface) around the peak stress (c) Stress-time and energy absorption-time curves (d) Element removal of yarns at 175 μ s

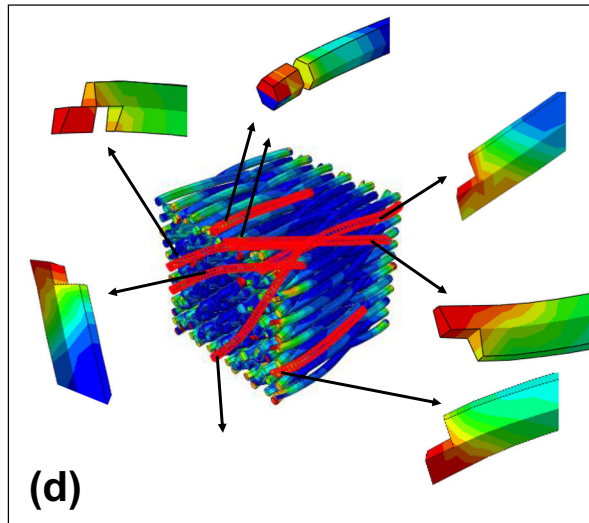
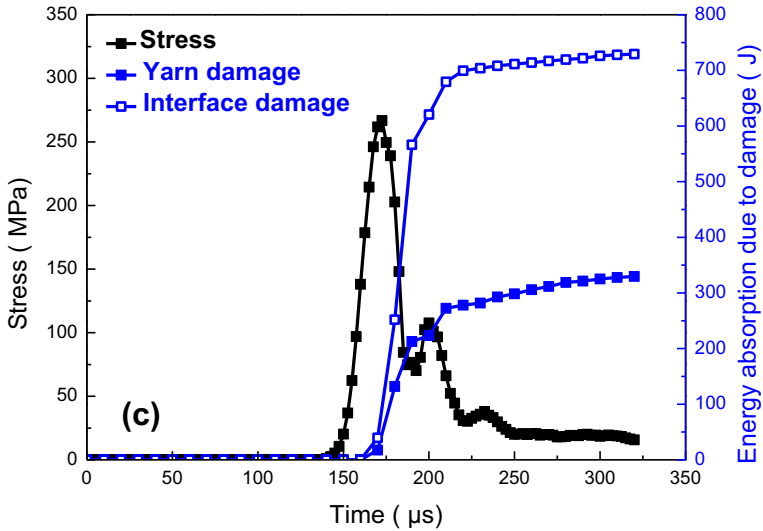


Fig. 4 (continued)

and the bars were meshed with the element type ‘C3D8R’. The results are insensitive to the mesh size based on our previous research [25]. Impact load was imparted on the end of incident bar. The displacement and rotation of bars were fixed in all directions except along impact direction.

4 Results and Discussion

Figure 3 shows the results obtained from experimental tests and simulation of each sample. A good agreement could be found. The characteristics of stress-strain curves, both peak load and

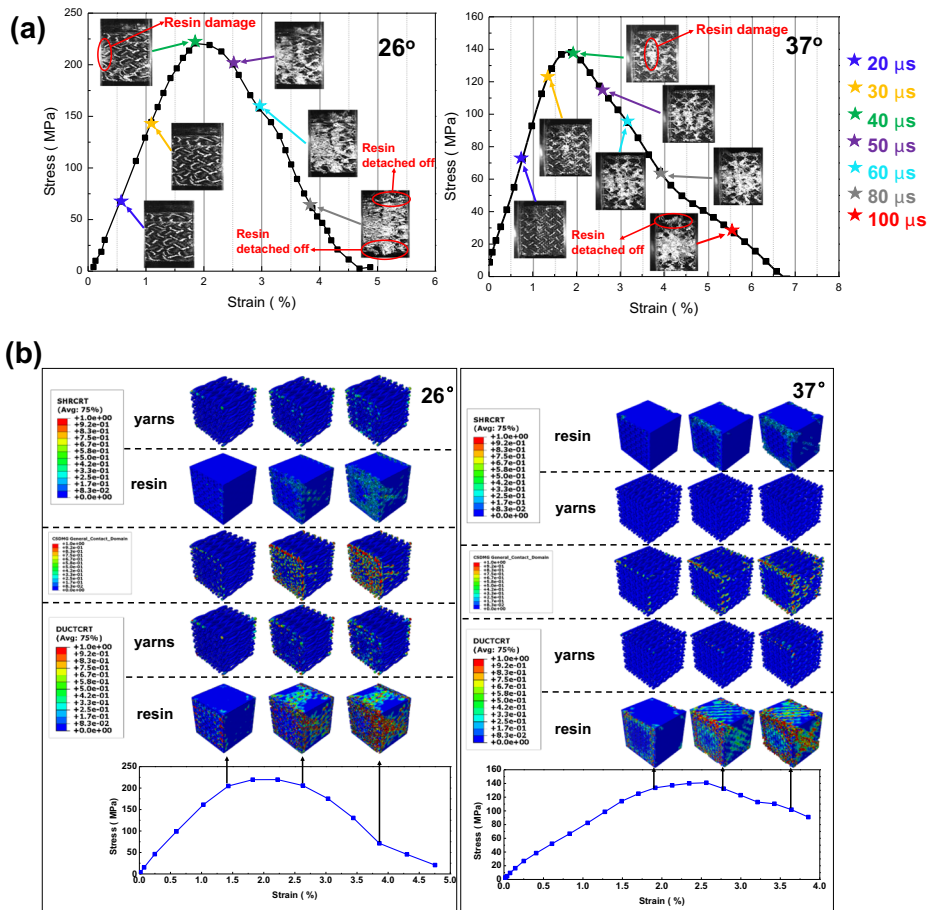


Fig. 5 Failure analysis of 26° and 37° sample at the first impact (a) Test results of damage evolution (b) Damage simulation of composite components (yarns, resin and interface) around peak stress (c) Stress-time and energy absorption-time curves (d) Stress variation on the yarns after resin damaged

modulus, are similar with the results from Zhao [14]. The damage morphology of samples during each impact pulse in experimental tests also matches well with the FEA result. The good agreement of both stress-strain curve and damage morphology proves the validity of model, which indicates that it can be used for further analysis.

4.1 Damage Evolution and Mechanisms

4.1.1 The First Impact

Figure 4a shows damage evolution of 15° sample during the first impact pulse. Damage initiation was observed at 40 μs in terms of crack appearance at yarn/resin interface when the stress drops off from the peak load. The stress continued to decreasing with the crack propagating through the damage sample to the area near transmission bar. Figure 4b shows the damage of individual components (reinforcement, resin and interface) around the peak stress. A noticeable damage appears at interface and yarns at the point the stress begins to drop.

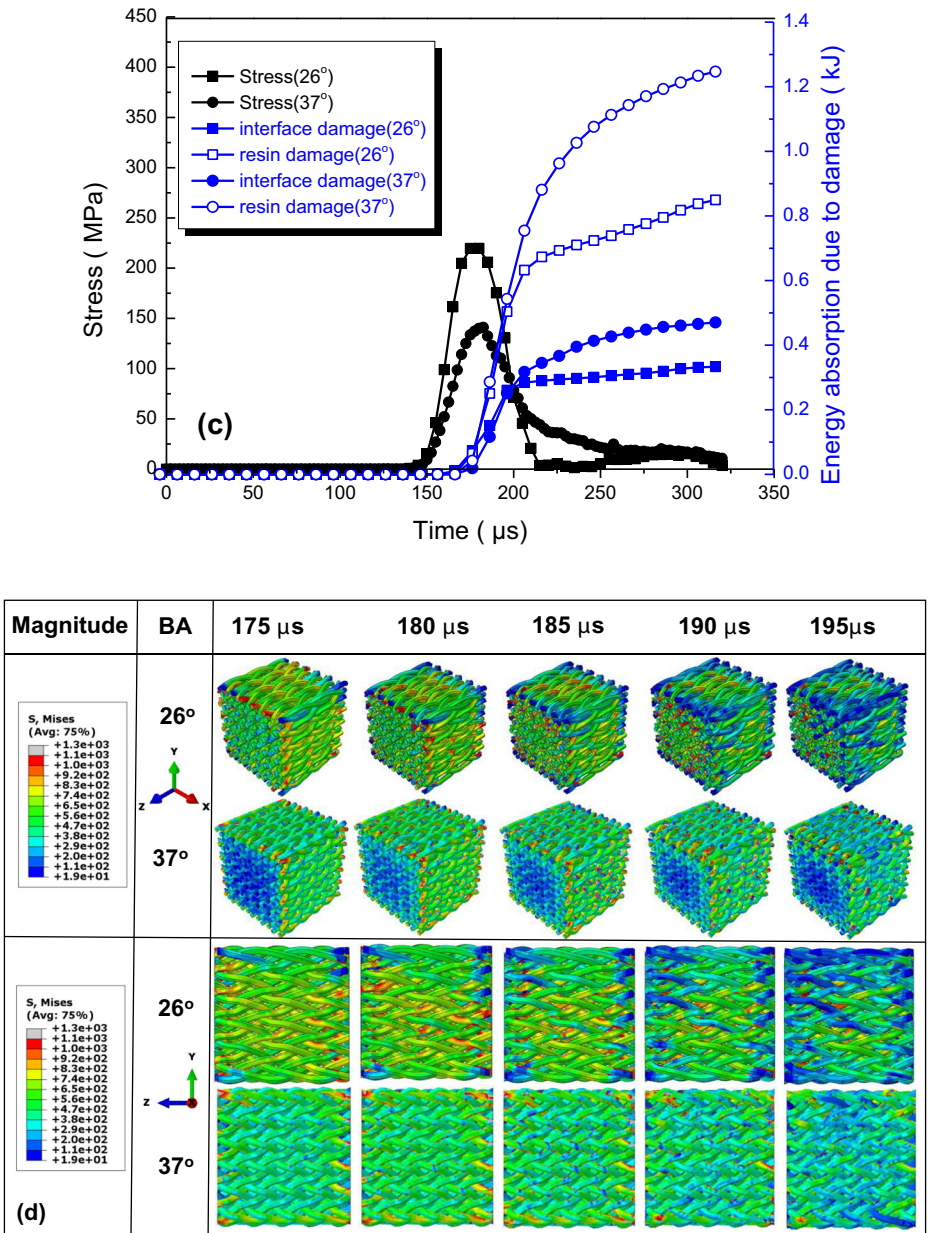


Fig. 5 (continued)

Gideon et al. also found interface debonding and fiber breakage are the main damage morphology for smaller braiding angle tube composite under axial fatigue load [37]. Figure 4c shows the stress-time as well as energy absorption-time curves. The energy absorption due to the stiffness degradation of yarns and interface is presented. It can be found that the drop of stress coincides with the rise of energy absorption curves. Meanwhile, the

elements removal of yarns is found at 175 μ s. Thus, it could be concluded that the failure for the 15° sample is resulted from the yarns and interface damage. This is different with the damage mechanisms under transverse impact load [31]. Under transverse impact load, it is the interface debonding and shears damages of resin that finally lead to the failure of the 15° sample.

Contrary to 15° sample, the damage initiated with resin fracture at 40 μ s and then the stress begins to fall down for 26° sample as shown in Fig. 5a. The fractured resin fragments which contribute to continuous drop of stress gradually moved apart from the sample. At 80 μ s, a huge amount of resin fragments has detached off from the surface of composite. The FEA results show that the interface also goes through pronounced damage when the stress decreases (Fig. 5b). Figure 5c shows stress-time and energy absorption-time curves. The energy absorbed due to stiffness degradation of resin and interface is presented. It can be seen that the stress-time curve starts to decline just at the time when energy absorption curves rise. Figure 5d shows the stress distribution on yarns for 26° and 37° sample after the resin has fractured. It can be seen that the stress of yarns gradually decreases because the damaged resin cannot support the yarns any more. Thus, the yarns bulked and final failure occurred. This damage process and tendency is also found in 37° sample as shown Fig. 5. This leads to the conclusion that the failure of the larger braiding angle samples (26° and 37°) is caused by resin and interface damage.

4.1.2 The Second Impact

Figure 6a presents damages during the second impact. For the 15° sample, the dislocation of adjacent yarns is very noticeable as highlighted by coloring the yarns. More debris of the fractured resin and yarns departs away from the sample. For the 26° sample, the angle between adjacent yarns becomes larger under impact. For the 37° sample, the yarns were squeezed much tighter. The failure mechanism schematic diagram is presented in Fig. 6b.

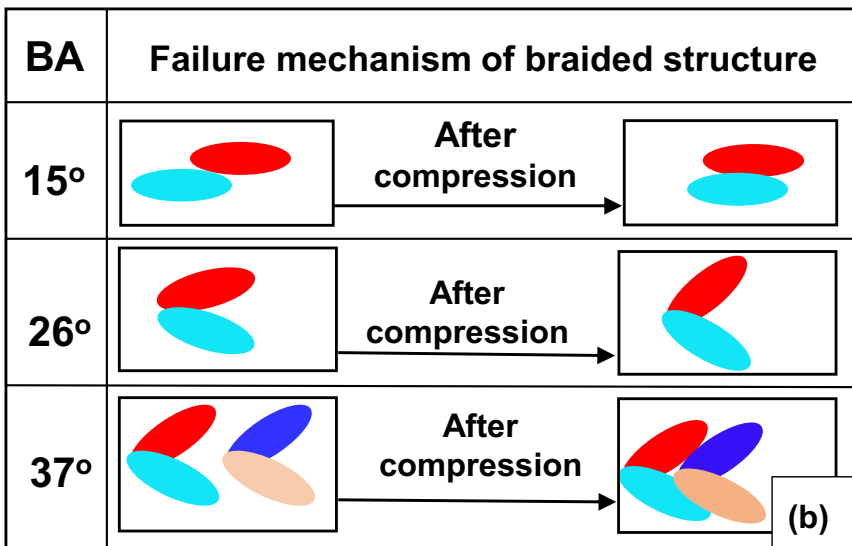
Figure 7a shows the displacement of yarns for each sample within the second impact. For 15° sample, the displacement of yarns is not the same among different regions of the braided structure. For 26° sample, the yarns at the end surface have the largest displacement and buckling deformation have occurred. For 37° sample, the braided structure seems tighter after the impact. The displacement of the end-surface region gradually increases with the impact load. Figure 7b shows the typical damage of the yarns for each sample during the impact process. For 15° braiding angle sample, the breakage and dislocation of yarn initiates during the first impact. The yarn goes on dislocating within the second impact as also observed from the experimental shown in Fig. 6a. This can partially account for the uneven deformation distribution in 15° braided structure. For the 26° sample, the braided yarn goes through multiple breakages within the second impact and buckling deformation developed around the breakage area, which finally leads to the increased angle between yarns. For the 37° sample, little breakage could be seen in the braided yarn.

4.1.3 The Third Impact

Figure 8 shows damage evolution during the third impact. The damage develops faster than the first and second impact due to stiffness degradation after the first and second impact. For the 15° sample, the braided structure breaks down. For the 26° sample, the angle between yarns

| BA | | 765 μs | 805 μs | 845 μs | 885 μs | 935 μs |
|-----|----------|-------------------|-------------------|-------------------|-------------------|-------------------|
| 15° | original | | | | | |
| | painted | | | | | |
| 26° | original | | | | | |
| | painted | | | | | |
| 37° | | | | | | |

(a)



(b)

◀ **Fig. 6** Damage evolution and schematic failure mechanism of braided preform at the second impact. **a** Damage evolution; **(b)** schematic damage mechanism (BA: Braiding Angle)

continues to increasing. For the 37° sample, it was compressed more tightly. The impact energy is almost dissipated up after the third impact.

4.2 Total Energy Absorption

Figure 9 shows the total energy absorption in each impact (E_t) and the ratio of energy absorption by each component to the total energy absorption by the entire composite (η). Total energy is the sum of energy absorption by the sample due to its elastic deformation, plastic deformation and stiffness degradation. η is given by the following expression.

$$\eta = \frac{E_c}{E_t} \quad (1)$$

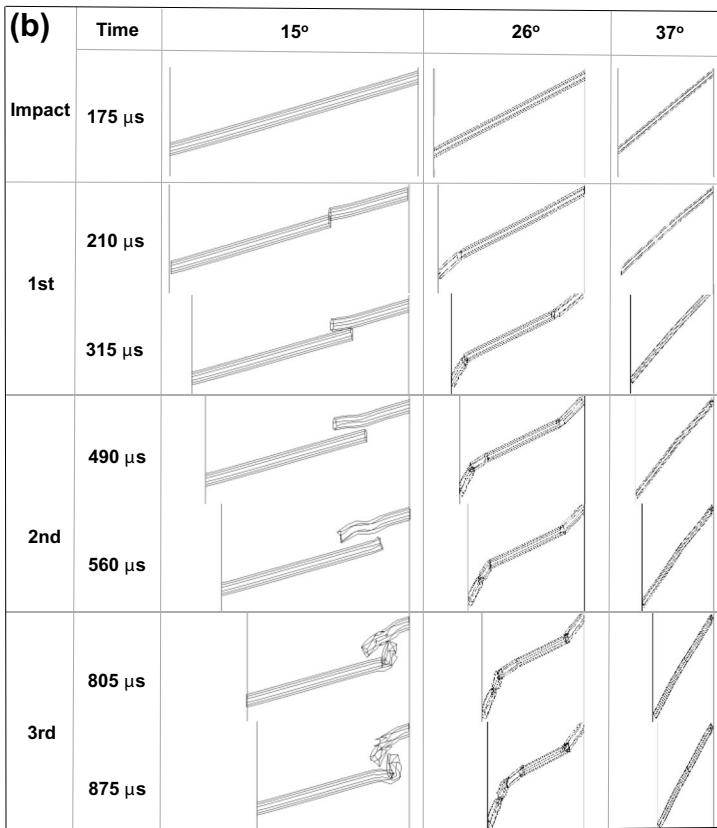
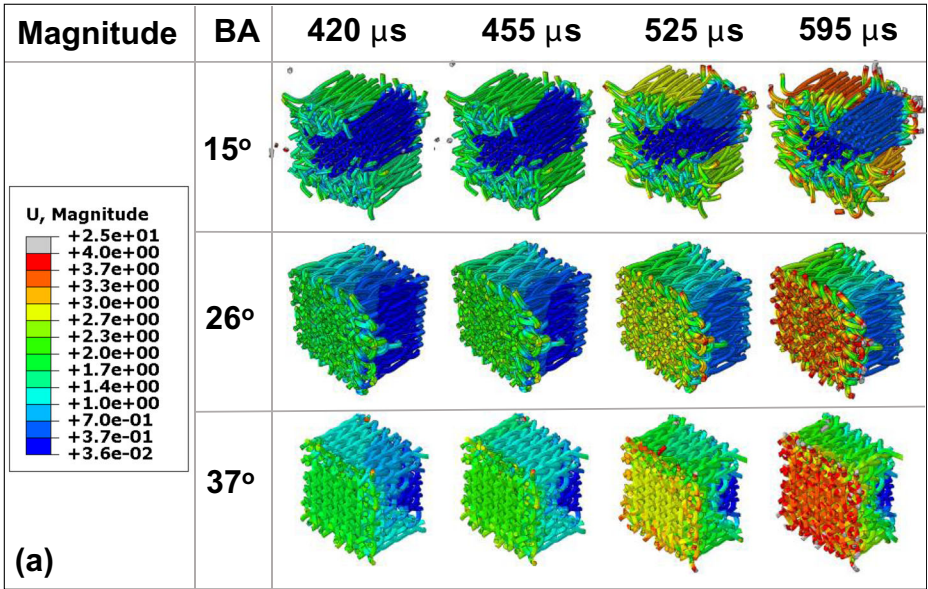
where E_c represents the energy absorbed by each component. E_t is the total energy absorption by composite. For the 15° sample, the η of yarns is higher than any other component during all three impacts. The yarns absorb 58.4% energy during the first impact, while 39.3% and 2.3% energy is absorbed by resin and interface, respectively. The η of braiding yarns increase to 78% and 79.1% during the second and third impact respectively, whereas the η of resin and interface reduce to less than 20% and 2% in the subsequent two impacts respectively.

For the 26° sample, the η of resin is 3.3% smaller than that of yarns at the first impact. The interface absorbs the least energy with a proportion of 2.5%. The η of yarns increase significantly at the second impact. The energy absorption ratio gap between yarn and resin widened to 60% at the second impact with 79.5% of yarns and 19.3% of resin. The η of the interface is still the smallest at the second impact with a value of about 1.2%. At the third impact pulse, the yarns are still the dominant energy absorption constituent with η of 78.6%. The η of the resin and interface is 20.2% and 1.2%, respectively.

For the 37° sample, the η of the resin is the highest at the first impact with an amount of 64%. The η of yarns and interface are 31% and 5%, respectively. At the second impact, the η of yarns increases to 37.5%, and it continues to rising to 74% at the third impact. The principal component for energy absorption of the 37° sample transferred from the resin at the first impact to the yarns at the third impact. This transformation trend was also found in transverse impact compression study [25].

For each sample, the η of yarns increases from the first impact to the third impact. This is because the resin damages quickly after the first impact. The yarns undertake more stress in the second and third impact. Then the η of the yarns also goes up.

It can also be found in Fig. 9 that the η of resin becomes higher as the braiding angle increased, especially at the first impact. This is because the stress undertook by yarns decreased with braiding angle and it increased for resin under longitudinal impact as shown in Fig. 10. This is just contrary to the result obtained from transverse impact compression [31]. In that impact direction, the stress undertook by yarns raised as the braiding angle and the η of resin decreased. The change of loading direction can result in completely different stress distribution in the samples.



◀ **Fig. 7** Deformation and failure of braided preform during impact process. (a) Displacement of yarns at the second impact; (b) Typical failure modes of yarns for each sample

4.3 Failure Modes

Figure 11 shows the energy absorption of each component due to its damage (E_d). For each sample, the E_d of resin is always the highest due to its poor strength except for the 37° sample at the 2nd and 3rd impact. For the 15° sample, the E_d of interface is less than the yarns at the first and third impact and almost equals to the yarns at the second impact. The E_d of each component decreases dramatically at the second and third impact, which indicates the less damage occurred.

For the 26° sample, the E_d of interface is higher than yarns at the first impact. It manifests that interface damaged more seriously than the yarns at the first impact. This is contrary to the result of the 15° sample. The more inclined yarns in the 26° sample is attributed to this difference. The stress on yarns reduced when the yarns got more inclined, which results in less yarn damage occurred than the interface. The E_d of the yarns and interface is nearly equal and very little at the subsequent two impacts, which indicates the little yarn and interface damage occurred.

In contrast to the 26° sample, the E_d of the yarns is higher than the interface at the first impact for the 37° sample. This is because the compact preform structure of the 37° sample makes yarns intend to squeeze each other rather than buckled in 26° sample. Thus, the E_d of the yarns is higher than interface. The E_d of yarns still maintains high magnitude at the second and third impact. This indicates that braided structure still undertakes certain load due to its good structural integrity. The damage of the yarns has become the dominant damage mechanism at the second and third impact.

It can be found in Fig. 11 that the yarns have been damaged significantly at the first impact regardless of braiding angles. This is also different with the result from transverse impact

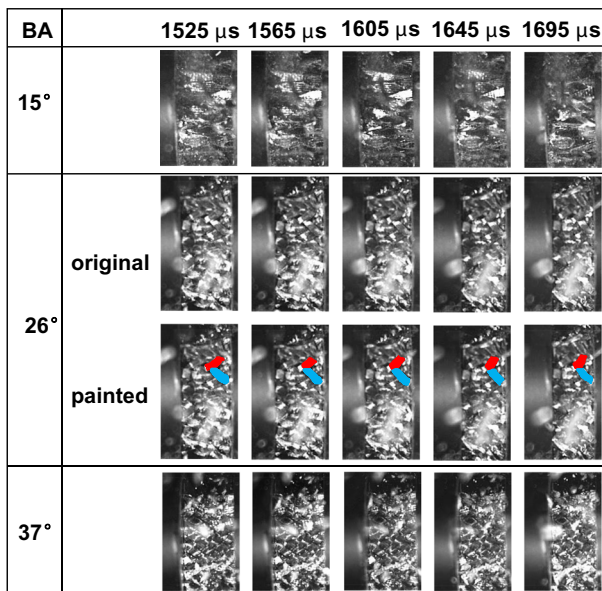


Fig. 8 Damage evolution of each sample at the third impact

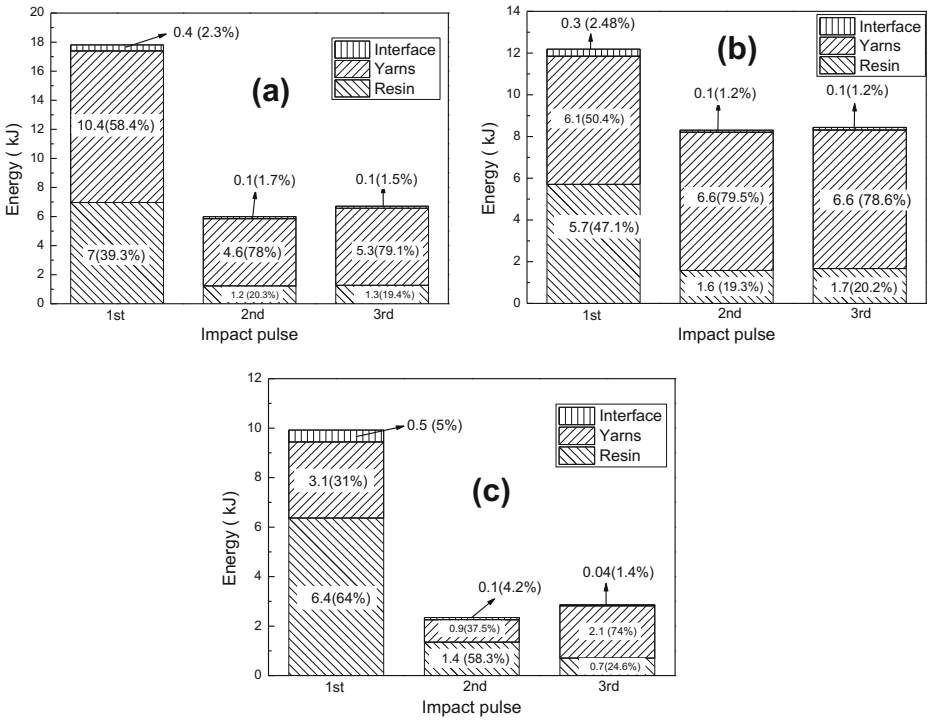


Fig. 9 Total Energy absorption of sample and absorption proportion of each component at every single impact (a) 15° braiding angle sample, (b) 26° braiding angle sample, (c) 37° braiding angle sample

compression [31]. Under transverse impact, the yarns are always most damaged at the second impact. This is because the yarn will not bear too much stress at the beginning under transverse impact. Under the longitudinal impact, the yarns share the most of impact load at the first impact.

Figure 12 shows failure modes of the yarns and resin at each impact. Ductile damage is the primary failure mode for both resin and yarns. The failure area of the resin is relatively

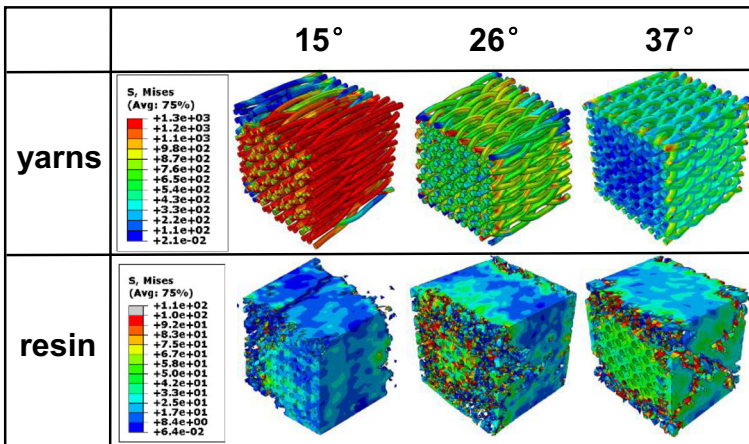


Fig. 10 Stress distribution on yarns and resin at the first impact

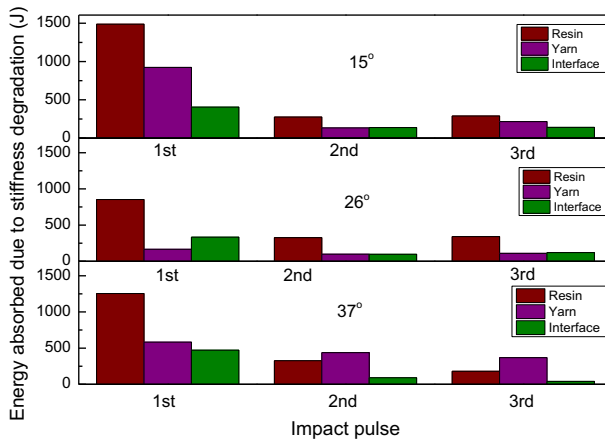


Fig. 11 Energy absorbed by each sample’s component due to its stiffness degradation at each impact

concentrated for the 15° sample compared to larger braiding angle samples (26° and 37° sample). The interface damage distributed similarly as the resin damage, concentrated for 15° sample, and more evenly for 26° and 37° sample as shown in Fig. 13.

5 Conclusions

We investigated the influence of braiding angle (i.e., 15°, 26° and 37°) on the multiple impact damages of 3-D braided composite under longitudinal direction. The impact damages were

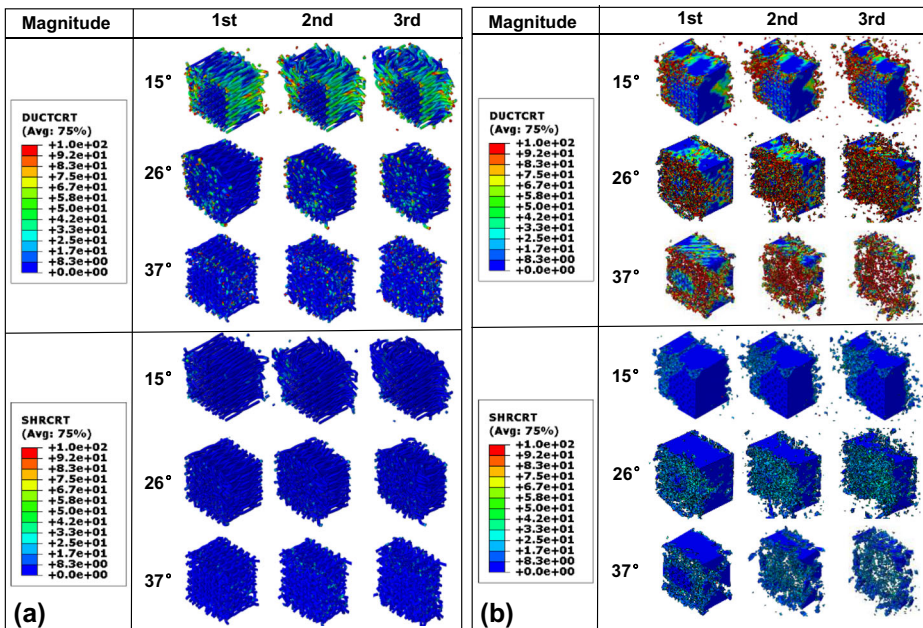


Fig. 12 Ductile and shear damage of (a) yarns and (b) resin at each impact

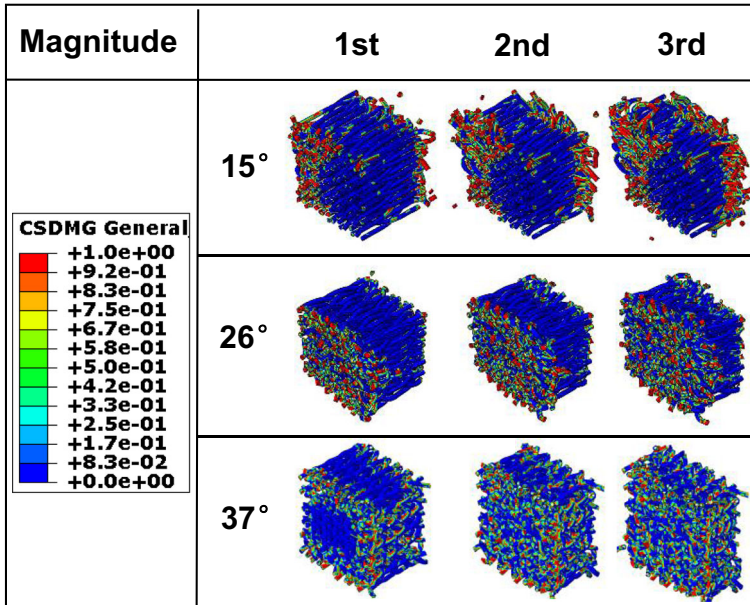


Fig. 13 Distribution of interface damage for each sample at every single impact

tested on a split Hopkinson pressure bar apparatus. The impact behaviors, including stress-strain curves, impact damages, were recorded and observed to analyze the impact damage behaviors. We also established a FEA model at meso-structural level to show the damage mechanisms. We have found that:

1. For the 15° sample, the damage of yarns is more serious than the interface at the first and third impact. The yarns and interface were damaged almost equally at the second impact. For the 26° sample, the interface damage was more serious than the yarns at the first impact. It goes through nearly identical damage for the interface and yarns at the second and third impact. For the 37° sample, the dominant damage component is resin at the first impact. It changed to the yarns at the second and third impact.
2. The proportion of energy absorption by yarns gradually increases from the first impact to the third. The proportion of energy absorption by the resin increases as braiding angle increases. The yarns are the dominant energy absorption component for smaller braiding angle sample while it changes to resin for the higher braiding angle sample.
3. The braiding angle influences the impact damages significantly along longitudinal direction. The samples with larger braiding angle maintain better structure integrity under multiple impacts, especially for the 37° sample. It could still undertake considerable load at the third impact. More investigations on the braiding angles could be conducted for revealing the impact damage mechanisms deeply.

Acknowledgements The authors acknowledge the financial supports from the Chang Jiang Scholars Program and National Science Foundation of China (Grant Number 51875099 and 51675095).

References

1. Wang, Y., Gao, X., Zhang, L., Wu, X., Wang, Q., Luo, C., Wu, G.: Synthesis of Ti₃C₂/Fe₃O₄/PANI hierarchical architecture composite as an efficient wide-band electromagnetic absorber. *Appl. Surf. Sci.* **480**, 830–838 (2019)
2. Wang, Y., Zhang, W., Wu, X., Luo, C., Wang, Q., Li, J., Hu, L.: Conducting polymer coated metal-organic framework nanoparticles: facile synthesis and enhanced electromagnetic absorption properties. *Synth. Met.* **228**, 18–24 (2017)
3. Zhang, H., Wang, B., Feng, A., Zhang, N., Jia, Z., Huang, Z., Liu, X., Wu, G.: Mesoporous carbon hollow microspheres with tunable pore size and shell thickness as efficient electromagnetic wave absorbers. *Compos. Part B.* **167**, 690–699 (2019)
4. Wang, J., Cai, K., Yin, J., Shen, S.: Thermoelectric properties of the PEDOT/SWCNT composite films prepared by a vapor phase polymerization. *Synth. Met.* **224**, 27–32 (2017)
5. Li, J., Ma, J., Chen, S., He, J., Huang, Y.: Characterization of calcium alginate/ deacetylated konjac glucomannan blend films prepared by Ca²⁺ crosslinking and deacetylation. *Food Hydrocoll.* **82**, 363–369 (2018)
6. Feng, A., Wu, G., Wang, Y., Pan, C.: Synthesis, preparation and mechanical property of wood Fiber-reinforced poly(vinyl chloride) composites. *J. Nanosci. Nanotechnol.* **17**(6), 3859–3863 (2017)
7. Kim, B.S., Hwang, B.S., Lee, S.K., Jun, E.J.: Development and trend of advanced polymer composites as structural materials in Korea. *Adv. Perform. Mater.* **5**(4), 353–361 (1998)
8. Ahmad, F., Choi, H.S., Park, M.K.: A review: natural Fiber composites selection in view of mechanical, light weight, and economic properties. *Macromol. Mater. Eng.* **300**(1), 10–24 (2015)
9. Sköck-Hartmann B, Gries T. Automotive applications of non-crimp fabric composites. 2011:461–480
10. McGregor, C., Vaziri, R., Poursartip, A., Xiao, X.: Axial crushing of triaxially braided composite tubes at quasi-static and dynamic rates. *Compos. Struct.* **157**, 197–206 (2016)
11. Li, Y., Gan, X., Gu, B., Sun, B.: Dynamic responses and damage evolutions of four-step three-dimensional braided composites subjected to high strain rate punch shear loading. *J. Compos. Mater.* **50**(12), 1635–1650 (2015)
12. Sun, B., Hu, H., Gu, B.: Compressive behavior of multi-axial multi-layer warp knitted (MMWK) fabric composite at various strain rates. *Compos. Struct.* **78**(1), 84–90 (2007)
13. Liu, L., Luo, G., Chen, W., Zhao, Z., Huang, X.: Dynamic behavior and damage mechanism of 3D braided composite fan blade under bird impact. *International J Aerospace Engineering.* **2018**, 1–16 (2018)
14. Zhao, Z., Liu, L., Chen, W., Huang, X.: Dynamic compressive behavior in different loading directions of 3D braided composites with different braiding angle. *Latin American J Solids and Structures.* **15**(9), (2018)
15. Zhang, W., Gu, B., Sun, B.: Transverse impact behaviors of 3D braided composites T-beam at elevated temperatures. *J. Compos. Mater.* **50**(28), 3961–3971 (2016)
16. Sun, B., Zhang, Y., Gu, B.: Low-velocity impact response and finite element analysis of four-step 3-D braided composites. *Appl. Compos. Mater.* **20**(4), 397–413 (2012)
17. McGregor, C., Vaziri, R., Xiao, X.: Finite element modelling of the progressive crushing of braided composite tubes under axial impact. *International J Impact Engineering.* **37**(6), 662–672 (2010)
18. Zhou, H., Li, C., Zhang, L., Crawford, B., Milani, A.S., Ko, F.K.: Micro-XCT analysis of damage mechanisms in 3D circular braided composite tubes under transverse impact. *Compos. Sci. Technol.* **155**, 91–99 (2018)
19. Zhang, Y., Wang, P., Guo, C.: Energy absorption behaviors of 3D braided composites under impact loadings with frequency domain analysis. *Polym. Compos.* **37**(5), 1620–1627 (2016)
20. Li, Y., Sun, B., Gu, B.: Impact shear damage characterizations of 3D braided composite with X-ray micro-computed tomography and numerical methodologies. *Compos. Struct.* **176**, 43–54 (2017)
21. Lai, J., Yang, H., Wang, H., Zheng, X., Wang, Q.: Penetration experiments and simulation of three-layer functionally graded cementitious composite subjected to multiple projectile impacts. *Constr. Build. Mater.* **196**, 499–511 (2019)
22. Wu, J., Liu, X., Zhou, H., Li, L., Liu, Z.: Experimental and numerical study on soft-hard-soft (SHS) cement based composite system under multiple impact loads. *Mater. Des.* **139**, 234–257 (2018)
23. Li, Q., Zhao, X., Xu, S., Leung, C.K.Y., Wang, B.: Multiple impact resistance of hybrid Fiber ultrahigh toughness cementitious composites with different degrees of initial damage. *J. Mater. Civ. Eng.* **31**(2), 04018368 (2019)
24. Zhou, H., Hu, D., Gu, B., Sun, B.: Transverse impact performance and finite element analysis of three dimensional braided composite tubes with different braiding layers. *Compos. Struct.* **168**, 345–359 (2017)
25. Gao, X., Sun, B., Gu, B.: Damage mechanisms of 3-D rectangular braided composite under multiple impact compressions. *Aerosp. Sci. Technol.* **82-83**, 46–60 (2018)
26. Mallick PK. *Fiber-Reinforced Composites: Materials, Manufacturing, and Design*: CRC press; 2007

27. Wan, F., Liu, R., Wang, Y., Sun, G., Cao, Y., Zhang, C.: Microstructure characterization and compressive performance of 3D needle-punched C/C–SiC composites fabricated by gaseous silicon infiltration. *Ceram. Int.* **45**(6), 6897–6905 (2019)
28. Luan, K., Liu, J., Sun, B., Zhang, W., Hu, J., Fang, X., Ming, C., Song, E.: High strain rate compressive response of the C/SiC composite. *Ceram. Int.* **45**(6), 6812–6818 (2019)
29. Zhang, F., Wan, Y., Gu, B., Sun, B.: Impact compressive behavior and failure modes of four-step three-dimensional braided composites-based meso-structure model. *International J Damage Mechanics.* **24**(6), 805–827 (2015)
30. Kolsky, H.: An investigation of the mechanical properties of materials at very high rates of loading. *Proceedings of the Physical Society Section B.* **62**(11), 676–700 (1949)
31. Gao X, Siddique A, Sun B, Gu B. Effect of braiding angle on dynamic mechanical properties of 3-D braided rectangular composites under multiple impact compressions. *J. Compos. Mater.* 2018;002199831881292
32. Li, D.S., Li, J.L., Chen, L., Lu, Z.X., Fang, D.N.: Finite element analysis of mechanical properties of 3D four-directional rectangular braided composites part 1: microgeometry and 3D finite element model. *Appl. Compos. Mater.* **17**(4), 373–387 (2010)
33. Hu, M., Zhang, J., Sun, B., Gu, B.: Finite element modeling of multiple transverse impact damage behaviors of 3-D braided composite beams at microstructure level. *Int. J. Mech. Sci.* **148**, 730–744 (2018)
34. Benzeggagh, M.L., Kenane, M.: Measurement of mixed-mode delamination fracture toughness of unidirectional glass/epoxy composites with mixed-mode bending apparatus. *Compos. Sci. Technol.* **56**(4), 439–449 (1996)
35. Huang, Z.M.: A unified micromechanical model for the mechanical properties of two constituent composite materials. Part IV: rubber-elastic behavior. *J. Thermoplast. Compos. Mater.* **13**(2), 119–139 (2000)
36. Zhang, M., Sun, B., Gu, B.: Meso-structure ageing mechanism of 3-D braided composite's compressive behaviors under accelerated thermo-oxidative ageing environment. *Mech. Mater.* **115**, 47–63 (2017)
37. Gideon, R.K., Zhou, H., Li, Y., Sun, B., Gu, B.: Quasi-static compression and compression–compression fatigue characteristics of 3D braided carbon/epoxy tube. *J Textile Institute.* **107**(7), 938–948 (2015)

Publisher's Note Springer Nature remains neutral with regard to jurisdictional claims in published maps and institutional affiliations.